Particle
& Particle Systems Characterization
www.particle-journal.com

In Situ Laser Light Scattering for Temporally and Locally Resolved Studies on Nanoparticle Trapping in a Gas Aggregation Source

*Jonas Drewes, Stefan Rehders, Thomas Strunskus, Holger Kersten, Franz Faupel, and Alexander Vahl**

Gas phase synthesis of nanoparticles (NPs) via magnetron sputtering in a gas aggregation source (GAS) has become a well-established method since its conceptualization three decades ago. NP formation is commonly described in terms of nucleation, growth, and transport alongside the gas stream. However, the NP formation and transport involve complex non-equilibrium processes, which are still the subject of investigation. The development of in situ investigation techniques such as UV–Vis spectroscopy and small angle X-ray scattering enabled further insights into the dynamic processes inside the GAS and have recently revealed NP trapping at different distances from the magnetron source. The main drawback of these techniques is their limited spatial resolution. To understand the spatio-temporal behavior of NP trapping, an in situ laser light scattering technique is applied in this study. By this approach, silver NPs are made visible inside the GAS with good spatial and temporal resolution. It is found that the argon gas pressure, as well as different gas inlet configurations, have a strong impact on the trapping behavior of NPs inside the GAS. The different gas inlet configurations not only affect the trapping of NPs, but also the size distribution and deposition rate of NPs.

1. Introduction

Noble metal nanoparticles (NPs) are used in many applications, ranging from catalysis,[1] photocatalysis,[2–4] optics,[5] and resistive switching[6–11] to sensors.[12–16] Especially the optical properties are well tunable because they depend strongly on the shape, size, size distribution, and the surrounding medium.[17,18]

A lot of synthesis methods for NPs are available and range from biological over chemical to physical processes.[19,20] The most often used strategy is the solution-based chemical synthesis. This approach has the drawback that the synthesized NPs are contaminated with, for example, surfactants.[19] Physical vapor deposition (PVD) techniques stand out with their extremely high purity of the synthesized NPs. Moreover, it is much easier to produce alloy particles and compound particles with tailored composition.[21] The PVD strategies range from surface energy-related self-organization of NPs on solid substrates[22–25] and in liquids[26–28]to gas phase synthesis.[8,29] The gas phase synthesis relies often on so-called gas aggregation sources (GASs). They encompass laser ablation,[29] pulsed microplasma cluster source,[8] and magnetron sputtering.[30] The GAS equipped with a magnetron was firstly developed by Haberland et. al. in 1992. Here a magnetron is operated at comparatively high pressures (typically between some 10 Pa and few 100 Pa) in contrast to normal magnetron sputtering for the preparation of thin films. Due to the higher pressure, the mean free path of the sputtered atoms is shorter, which enables three-body collisions (two sputtered atoms are colliding with one gas atom) and leads to the formation of dimers.[31] This enables further attachment of sputtered atoms, and the dimers can grow further to clusters and NPs. These NPs are guided by the drag force due to the gas flow outside the GAS into the deposition chamber, where they can be deposited onto various substrates.[30]

Although the fundamental three-body collision process and consecutive nucleation, growth, coalescence, and transport are well discussed in literature, still not all ongoing processes inside such sources are completely understood. For example, the impact of the gas flow pattern inside a GAS was for a long time only superficially investigated. Nevertheless, previous studies have shown that

J. Drewes, S. Rehders, T. Strunskus, F. Faupel, A. Vahl
Chair for Multicomponent Materials
Institute of Materials Science
Kiel University
Kaiserstr. 2, D-24143 Kiel, Germany
E-mail: alva@tf.uni-kiel.de

T. Strunskus, H. Kersten, F. Faupel, A. Vahl
Kiel Nano
Surface and Interface Science KiNSIS
Kiel University
Christian-Albrechts-Platz 4, D-24118 Kiel, Germany

H. Kersten
Chair for Plasma Technology
Institute of Experimental and Applied Physics
Kiel University
Leibnizstr.19, D-24098 Kiel, Germany

The ORCID identification number(s) for the author(s) of this article can be found under https://doi.org/10.1002/ppsc.202200112.

© 2022 The Authors. Particle & Particle Systems Characterization published by Wiley-VCH GmbH. This is an open access article under the terms of the Creative Commons Attribution-NonCommercial License, which permits use, distribution and reproduction in any medium, provided the original work is properly cited and is not used for commercial purposes.

DOI: 10.1002/ppsc.202200112

15214117, 2022, 11, Downloaded from https://onlinelibrary.wiley.com/doi/10.1002/ppsc.202200112 by Universitatsbibliothek Kiel, Wiley Online Library on [19/05/2023]. See the Terms and Conditions (https://onlinelibrary.wiley.com/terms-and-conditions) on Wiley Online Library for rules of use; OA articles are governed by the applicable Creative Commons License

the gas flow pattern inside a GAS plays a crucial role.[32–36] For example if low-velocity regions are present inside a GAS, NPs can get lost in the chamber walls or the target.[36] This effect strongly impacts the material conversion efficiency of a GAS.

To improve the performance of GAS sources, in the last decade several in situ techniques were utilized already to analyze the growth and transport of NPs inside the GAS. Examples are in situ small angle X-ray scattering (SAX)[37,38] and in situ UV–Vis.[33,36] Both techniques provided further insights into the dynamic processes inside the GAS and have revealed NP trapping at different distances from the magnetron source. Even though these techniques can provide information about the NP size, the techniques suffer from their low spatial resolution.

Therefore, a technique with good spatial and temporal resolution to investigate the processes inside the GAS is urgently needed. Different laser light scattering (LLS) techniques have been successfully used to investigate NP growth and transport in situ in plasmas but not inside a GAS. Some methods rely on Mie scattering[39–41] and others on Rayleigh scattering.[42–45] Mie scattering techniques are Mie ellipsometry, angular-resolved Mie scattering, and 2D imaging Mie ellipsometry. By these methods, NPs of radii between 80–200 nm can be detected, for example, inside a dusty plasma. By evaluation of the polarization also the size distribution of the NPs can be evaluated in situ inside the plasma.[39–41] The limit for the NP diameter between Mie scattering and Rayleigh scattering is about 1/10 of the wavelength. Because the usual size of NPs which are prepared with a GAS is typically below 50 nm and the wavelength of the applied laser is 532 nm, Mie scattering techniques are not applicable to the GAS.

Therefore, in this study LLS based on Rayleigh scattering has been used. A laser plane through the GAS is created and in a 90° configuration a camera with color filter is mounted to the GAS. The scattered light by the NPs can be detected and so the location of NPs inside the GAS can be observed. In this way the LLS technique was often used in conventional RF dusty plasmas but not in a GAS.[42–45] Here no information about the size distributions can be found, but other techniques like in situ SAX or in situ UV–Vis can provide this information. However, they cannot provide precise information about the location of NPs. For that reason, LLS can be seen as a complementary tool to understand the ongoing processes inside a GAS.

Here, LLS of Ag NPs will be utilized to extract better spatial information about the trapping positions of NPs inside a custom-built GAS based on a typical design. To study the impact of the Ar gas flow pattern on the NP formation and transport process, three different types of gas inlets are investigated. The results from the LLS for different gas inlets will be complemented by size distributions obtained by scanning electron microscopy (SEM) measurements of the deposited NPs and the measured deposition rates.

2. Experimental Section

2.1. Setup of the Experiment

In typical gas aggregation deposition experiments, the GAS sources have commonly only 4 flanges. In this common 4-flange-setup, one flange was used to attach the magnetron and one flange (on the opposite side) was used for the orifice. Additionally, two ports perpendicular to the main axis of the GAS were used for analytical purposes.[21,33,37,38,46] Computational fluid dynamic simulations (CFD) have shown that additional ports, which do not taper the cross-section of the GAS, do not significantly influence the gas velocity distribution.[33,46] Therefore, additional analytical ports were considered uncritical for the growth and transport of NPs. For this study more than two analytical ports were needed, which motivated the choice to build a GAS based on a CF 63 cross with 6 ports (**Figure 1**). On the back-left port, a 2-inch custom-made magnetron was mounted. The design of the magnetron was based on the "Ionix" magnetron series from the company Thin Films Consulting. On one of the ports (front right in Figure 1a) a cone with a 3 mm orifice was installed and connected to the deposition chamber. Two other ports of the GAS, which were located directly next to each other, were equipped with glass windows for the optical scattering system. On the remaining ports, the pressure gauge and a blind flange were installed. The deposition chamber was equipped with a QCM (Quartz Crystal Microbalance) and load-lock, which enables fast sample transfer without breaking the vacuum.

The GAS was mounted to the deposition chamber. The orifice connects the GAS and the deposition chamber. The deposition chamber was evacuated by a turbo pump (Pfeiffer, HiPace 60 P) with a scroll fore pump (Edwards, nXDS 6i). The base pressure is in the range of 10^{-7} mbar. The loadlock was equipped with a turbo pump (Pfeiffer, TMU 071 P) with a scroll fore pump (Edwards, nXDS 6i). The gas flow was controlled via mass flow controller (MKS Instruments, 1179BX22CM1BV, 200 sccm range of N_2). The used Ar gas flows are 109.6, 137.0, 164.4, 191.8, and 219.2 sccm with the corresponding pressures in the GAS of 118, 141, 163, 183, and 204 Pa, respectively.

The custom-made magnetron enables three different gas inlet configurations. Therefore, the original design of thin Films consulting was professionally overhauled. The three different inlet configurations are shown in Figure 1b. The first configuration was termed normal inlet based on the default design of thin Films Consulting. In the normal inlet configuration, the gas was injected into the chamber between the magnetron and the ground cap. The custom-made magnetron used here enables the gas to be injected through the middle of the target. This is called middle inlet. Here the difficulty was to guide the Ar gas between the ground cap and the magnetron and finally under the target through the central bore (5 mm diameter) inside the target. It was important to prevent large stagnation pressures between the magnetron and the ground cap, because this can cause plasma ignition at this undesired point. The bore was closed with a stainless-steel mesh on the same electrical level as the target surface. Otherwise, plasma ignition can take place inside the bore. The third inlet configuration was the behind inlet configuration, which can be often found in literature.[33,37,38] Here the gas inlet was located somewhere behind the magnetron. Ag was always used as a target material (99.99% purity, Kurt J. Lesker, 2 inch)).

An MDX 500 from Advanced Energy supplies the DC power to the magnetron. It was used in the power regulation mode, which is always set to 300 W.

 © 2022 The Authors. Particle & Particle Systems Characterization published by Wiley-VCH GmbH

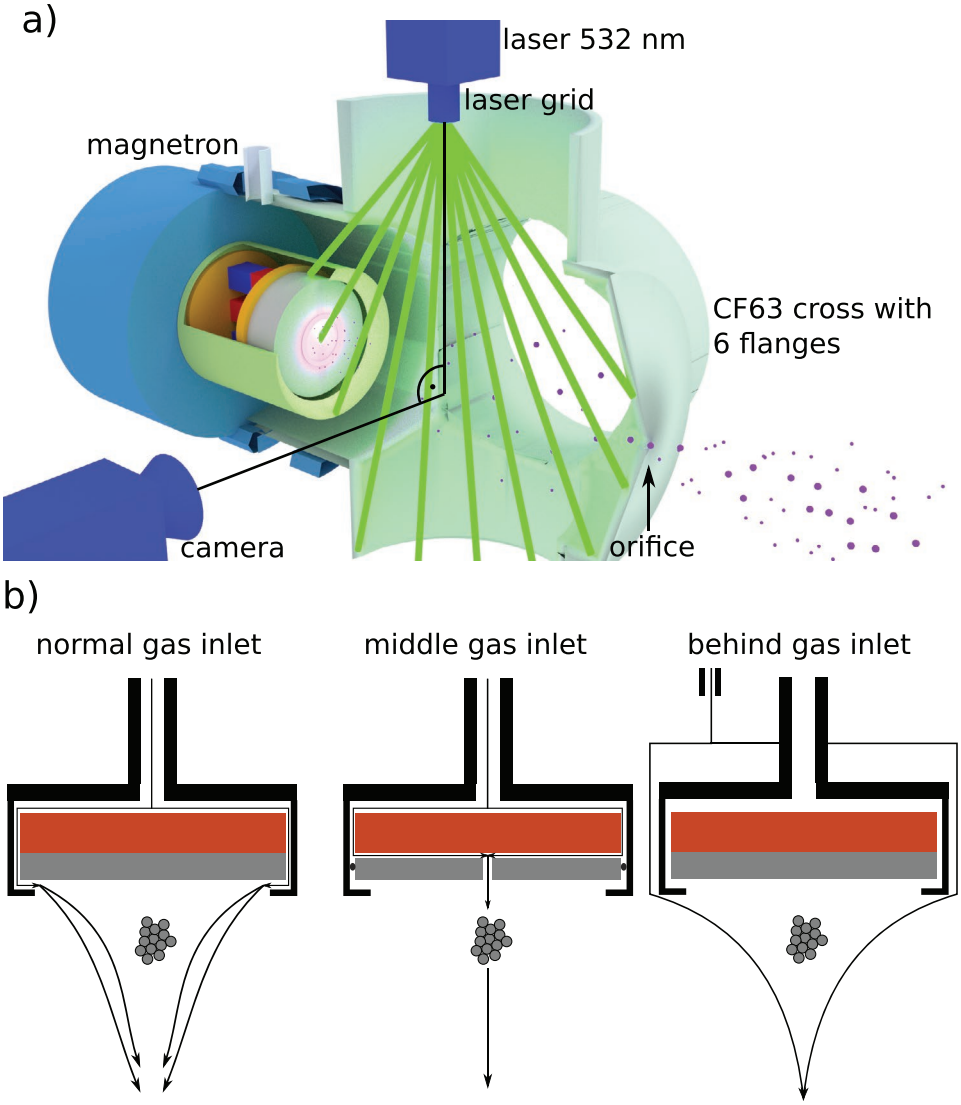

Figure 1. a) Measurement setup for the in situ laser scattering experiments in the GAS. The GAS is based on a CF63 cross with 6 flanges. On the back left flange, the magnetron is mounted. On two side flanges, two windows are mounted. On one window the camera with a color filter for green light is mounted and on the other window the laser. The laser beam is split by a grid so, that the plane from the center of the magnetron to the orifice is illuminated. b) The three different types of gas inlets are shown. For the normal gas inlet, the gas is inserted between the magnetron and the ground cap so that the gas is directed onto the target surface. The middle gas inlet means that the gas is injected through the middle of the target. The third gas inlet configuration is termed behind inlet, which means that the gas is injected somewhere behind the magnetron and the gas flows around the ground cap.

The scattering system consists of a laser with a wavelength of 532 nm with a power of 450 mW (Roitner Laser Technik, RLTMGL-532 1–450 mW) and a CMOS camera (XIMEA, MQ042CG-CM), with a color filter, which transmits light with a wavelength of 532 nm but blocks most of the light with different wavelength, which was generated by the plasma. The framerate of the camera was fixed at 25 frames per s. In front of the laser, a grid was installed which created out of the single beam a laser plane under an opening angle of 30°. The laser and the camera were installed under a 90° angle, and the laser plane includes the center line from the target to the orifice and lies normal to the camera (Figure 1).

For SEM investigations, NPs were deposited inside the vacuum chamber at a distance of 16 cm from the GAS exit orifice. Here, as substrate material, p-doped, (100) oriented Si wafer pieces with native oxide (cut to $1 \times 1\,cm^2$, SiMat) were used. The SEM analysis was done with a Zeiss Ultra Plus microscope.

2.2. Image Formation

First, the image formation and the image processing will be described. In general, three different effects were contributing to the recorded raw image of the camera: The reflections of the incident laser light from the chamber walls, the plasma emission, and the scattered light from the NPs. The latter one contains the information about the location of NPs, which was of interest for this study.

© 2022 The Authors. Particle & Particle Systems Characterization published by Wiley-VCH GmbH

15214117, 2022, 11, Downloaded from https://onlinelibrary.wiley.com/doi/10.1002/ppsc.202200112 by Universitatsbibliothek Kiel, Wiley Online Library on [19/05/2023]. See the Terms and Conditions (https://onlinelibrary.wiley.com/terms-and-conditions) on Wiley Online Library for rules of use; OA articles are governed by the applicable Creative Commons License

Particle & Particle Systems Characterization
www.particle-journal.com

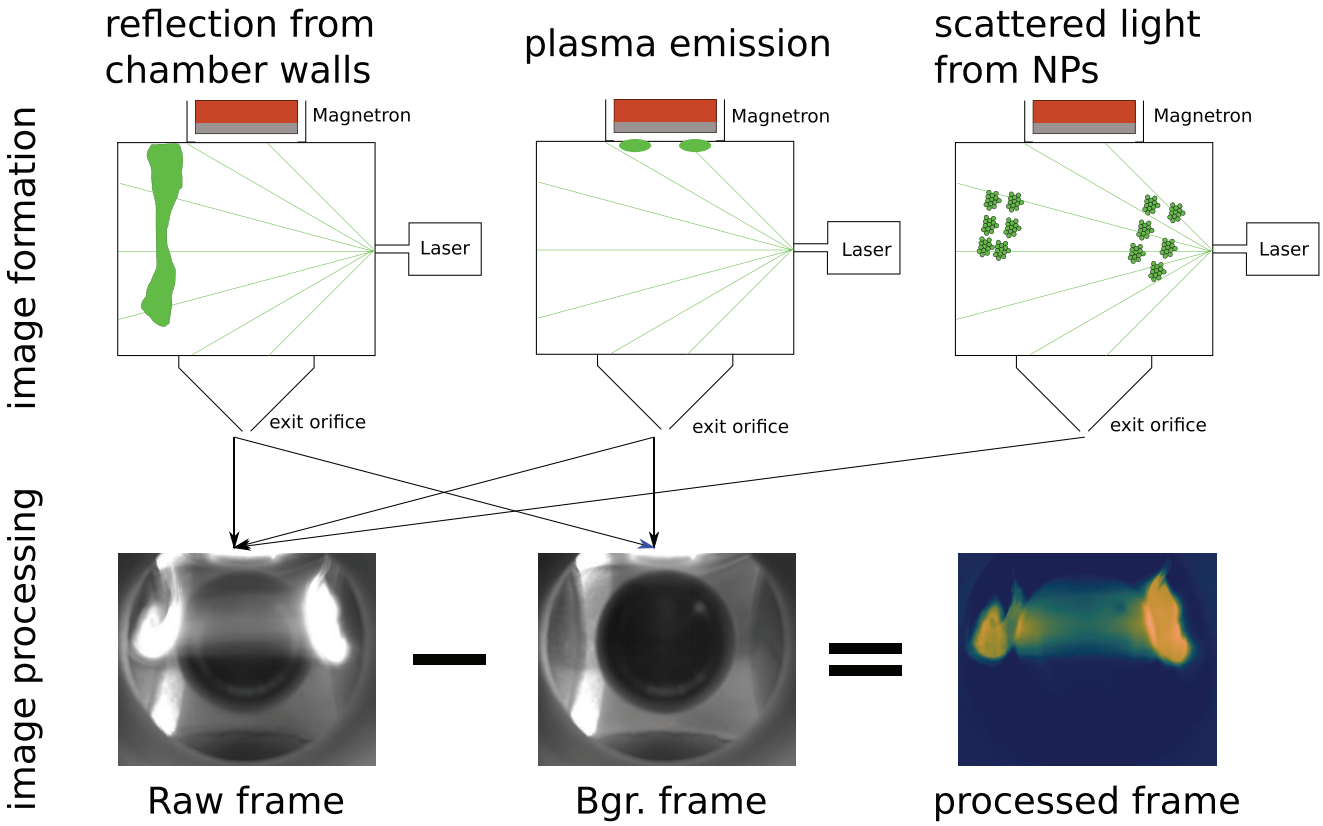

Figure 2. Schematic of image formation and image processing by the Matlab script. In the top row, the three light contributions inside the chamber are shown: Reflection from chamber walls, plasma emission, and the scattered light from NPs. In the bottom row, the video processing by the Matlab script is illustrated. The arrows from the top to the bottom row are visualizing the contributions from the different light sources into the raw frame and the background frame.

Information about the locations of NPs can be obtained due to the Rayleigh scattering phenomenon. The Rayleigh scattering equation tells us that the scattering Intensity (I) depends on the particle size (a), the refractive index of the medium (n_{med}), the intensity of the incident light (I_0), the distance from the scattering object to the detector (d), the wavelength of laser light in vacuum (λ), the particle relative refractive index (m), and the test angle (θ):[47]

$$I = \frac{8\pi^4 a^6 n_{\text{med}}^4 I_0}{d^2 \lambda_0^4} \left| \frac{m^2 - 1}{m^2 + 1} \right|^2 \left(1 + \cos^2 \theta\right) \quad (1)$$

For the LLS method, the two most important varying parameters were the particle size and particle density. The scattering equation shows that the scattering intensity depends on particle size to the sixth power. Since this equation gives the scattering intensity for one particle, the scattering intensity depends only linearly on the particle density. The dependence on the size of the NPs and the particle density was important for the interpretation of the LLS images.

The different contributions to the raw image are schematically shown in **Figure 2**. The plasma emission and the reflections from the chamber walls do not contain the desired spatial information about the NPs. Therefore, the videos have to be processed after the experiments before further analysis. The color filter used in front of the camera already filters out the main portion of the plasma emission but still, a small portion contributes to the image. Since the chamber walls were curved, always some reflected laser light can enter the camera. In the end, the remaining plasma emission and the reflected light from the chamber walls have to be subtracted to obtain the information about the location of the NPs. This was done with a Matlab script and will be described in detail in the next chapter.

2.3. Image Recording and Processing

To extract only the signal of NPs out of the video, a MatLab script was used to subtract the emission and the scattered light from the chamber walls. The procedure was as follows: The camera recording was started prior to the experiment. The program detects the start of the plasma discharge and synchronizes the recording of the camera with the plasma ignition. Half a second after the plasma was ignited a background frame was taken. This frame contains the plasma emission and the reflected light from the chamber walls but no signal from NPs. A previous study has shown that it takes some seconds until NPs were detected inside a GAS.[36,38] For that reason, half a second was chosen for the background frame. This background frame was subtracted afterwards from the whole video. Then

© 2022 The Authors. Particle & Particle Systems Characterization published by Wiley-VCH GmbH

15214117, 2022, 11, Downloaded from https://onlinelibrary.wiley.com/doi/10.1002/ppsc.202200112 by Universitatsbibliothek Kiel, Wiley Online Library on [19/05/2023]. See the Terms and Conditions (https://onlinelibrary.wiley.com/terms-and-conditions) on Wiley Online Library for rules of use; OA articles are governed by the applicable Creative Commons License

the program transfers the video into a color plot to increase the visibility in comparison to a mono-colored picture (Figure 2). In addition, the program sums up all pixel values for each frame after the background subtraction. These summed-up values are called cumulative intensity and can be plotted over time to analyze the temporal development of the intensity within one experiment. Furthermore, one can integrate over the whole experimental time to obtain the total intensity of one experiment to compare experiments with each other.

3. Results and Discussion

This study is structured in four different sections. In the first section, the temporal changes in the spatial distribution of NPs inside the GAS will be discussed for one gas inlet configuration with a specific flow. By this example, the dynamic processes inside the GAS will be visualized and discussed. In the second part, the spatial NP distribution inside the GAS for three different gas inlets and five different gas flows and pressures will be evaluated. The aim is to study the influence of GAS geometries and different gas flow patterns on the trapping behavior of NPs inside the GAS. In the third section, the change in the size distribution of the deposited NPs will be discussed to understand the dependence between the growth processes of NPs and the gas flow pattern. In the last section, the impact of different gas inlets and pressures on the deposition rate will be analyzed to understand the impact of different gas inlets and flows on the efficiency of the NP synthesis.

3.1. Dynamic Processes of NP Formation and Transport

In the first part of this study, an exemplary typical LLS image time series for the middle inlet configuration will be discussed. **Figure 3**a shows schematically how the magnetron, the laser, and the exit orifice are located in relation to the field of view of the camera. Within this field of view, different features can be

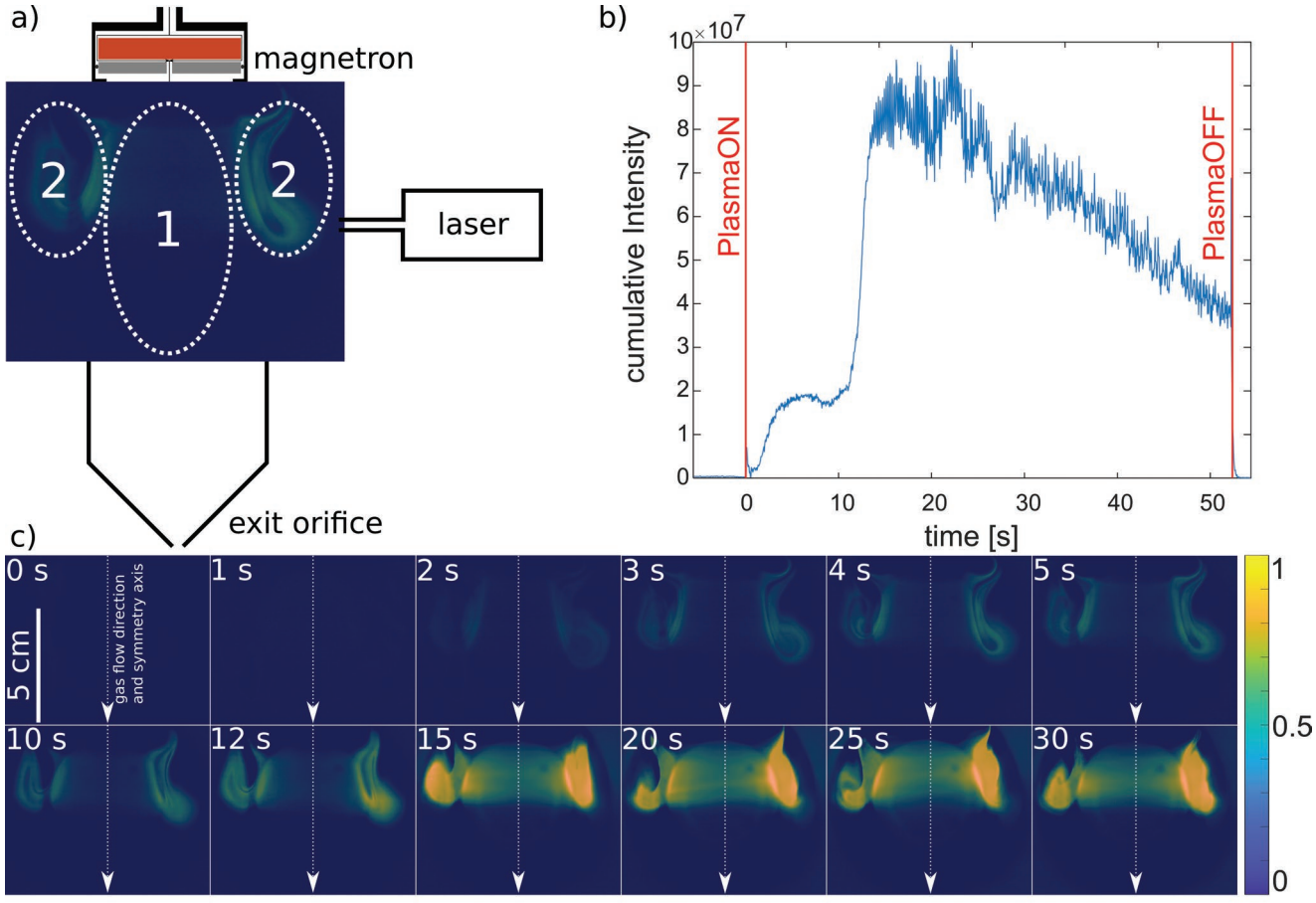

Figure 3. a) Left the position of the magnetron and the orifice are schematically drawn into an exemplary LLS image to clarify where the NPs are in comparison to the magnetron and the orifice. Moreover, three different regions are labeled inside the LLS image. The edge regions (marked as 2) are located left and right and the center region (marked as 1) in the middle of the LLS image. b) The plot shows on the x-axis the time and on the y-axis the cumulative intensity. The cumulative light intensity is the sum of all pixel values from the whole picture. It first increases until ≈7 s before it reaches a local maximum and shortly decreases until ≈10 s. Then it increases further until ≈15 s and then decreases until the plasma is switched OFF. c) LLS images for the middle inlet configuration with a pressure of 183 Pa for 0, 1, 2, 3, 4, 5, 10, 12, 15, 20, 25, and 30 s after the plasma is switched on. It is visible, that the intensity is increasing over time, indicating growth of NPs or increasing NP density. The NPs are trapped only in the edge regions of the GAS and it appears to have a vortex-like shape. Additionally, the dotted arrows are indicating the gas flow direction and the symmetry axis of the GAS.

© 2022 The Authors. Particle & Particle Systems Characterization published by Wiley-VCH GmbH

15214117, 2022, 11, Downloaded from https://onlinelibrary.wiley.com/doi/10.1002/ppsc.202200112 by Universitatsbibliothek Kiel, Wiley Online Library on [19/05/2023]. See the Terms and Conditions (https://onlinelibrary.wiley.com/terms-and-conditions) on Wiley Online Library for rules of use; OA articles are governed by the applicable Creative Commons License

15214117, 2022, 11, Downloaded from https://onlinelibrary.wiley.com/doi/10.1002/ppsc.202200112 by Universitatsbibliothek Kiel, Wiley Online Library on [19/05/2023]. See the Terms and Conditions (https://onlinelibrary.wiley.com/terms-and-conditions) on Wiley Online Library for rules of use; OA articles are governed by the applicable Creative Commons License

observed. These include the center region in the middle of the picture (marked as 1) and the edge regions left and right in the image (marked as 2). Directly after starting the magnetron discharge, the NP formation process is far away from equilibrium, as at 0 s there are no nuclei or preformed particles in the source. Therefore, the early stages of the gas phase synthesis are particularly interesting to study. For this reason, the time period between 0 and 5 s is depicted in detail in Figure 3c. The time 0 s corresponds to the moment where the plasma is switched on. After 2 s scattered light from the NPs becomes visible and the intensity is increasing up to 15 s. Not only the intensity is increasing over time but also the shape and the dimensions of the trapped NPs in the edge regions are changing. The NP cloud looks like vortexes are present. The vortex behavior is much more visible in the processed videos. Therefore, one video for each inlet configuration can be found in the supporting information. In Figure 3c only at the edge regions, NPs are visible and not in the center regions. Additionally, the image series shows that the growth and transport of NPs inside the gas is a highly dynamic process. Finally, Figure 3b shows the cumulative intensity of the whole LLS image over time. This means that all pixel values of the images are summed up for each frame. This plot indicates also that the processes of NP formation and transport inside the GAS are time-dependent. In the beginning, the cumulative intensity is increasing until ≈5 s before it reaches a local maximum and shortly decreases until ≈10 s. Then it increases further until ≈15 s and then decreases until the plasma is switched off. That the intensity increases, in the beginning, is due to the NP formation and further growth of these NPs, which can be also seen in the LLS images from 0 to 5 s. The decrease is caused by fewer NPs or smaller NPs, respectively. Since the Rayleigh scattering depends strongly on the size of the NPs (to the power of 6) but also on the number of particles, this method cannot distinguish between the impact of size and number of NPs (discussed in detail in Section 2.3). One other reason could be that the NPs are simply moving in and out of the inspected region which is related to the small width of the laser plane. By the example of the time series of LLS images, it is presented how complex the NPs' growth and transport behavior in GAS is. Since prior to the deposition no metal atoms and no NPs are present in the gas phase it will take a certain time until it is possible, that nucleation, cluster growth, and transport of NPs out of the growing region are in a steady state. Perhaps a stable steady state can never be reached, because of the fast kinetics and also increasing temperature of the chamber walls. Nevertheless, the fundamental features of the LLS image stay relatively constant over the whole deposition time, which indicates that the NPs are trapped by an interplay out of drag forces and electromagnetic forces. This is in line with earlier reports on trapping of NPs inside the GAS.[33,34,36–38]

In these earlier studies, techniques like in situ UV–Vis or in situ SAX were used to analyze the growth and transport of NPs. These techniques average data out of the whole interaction volume of the light beam or X-ray beam. In comparison to these studies, LLS has the distinct advantage, that the signal originates from one two-dimensional plane out of the GAS. This enables the exact localization of NPs inside the GAS although the size and the number of NPs cannot be evaluated. Also, the fact that the cumulative intensity drops down extremely fast after the switch-off, shows that the NP trapping must be related to electromagnetic forces which are missing when the plasma is switched off. Assuming the NPs are trapped only because of turbulences inside the gas flow, the NPs would still stay in the turbulences when the plasma is switched off because the gas flow is not much affected by the plasma. The fact that the NPs are immediately vanishing when the plasma is switched off indicates trapping due to the interplay of electromagnetic forces and drag force.[33]

3.2. Impact of Gas Inlet and Gas Flow/Pressure on the NP Trapping Behavior

After having discussed the fundamental features of the dynamic phenomena after starting the gas phase synthesis of NPs, in the following section it will be shown how different gas inlet configurations and different Ar gas flows and pressures will change the trapping behavior of the NPs inside the GAS. **Figure 4** shows 15 LLS images taken after 30 s of operation and all with the same discharge power. 30 s were chosen because the gas phase synthesis process approaches an equilibrium, where the relative intensity distribution between the different trapping locations does not change significantly over time. Each row corresponds to one pressure and gas flow, which is increasing from left to right. Each line corresponds to one inlet configuration: first the middle configuration, then the normal inlet configuration, and in the last row the behind configuration. The first point to make is that the intensities for all inlet configurations are increasing with an increase in gas flow/pressure. This can be caused by more efficient NP nucleation at higher pressures which produce more NPs.[48] One can also distinguish between two different trapping regions. One is located at the edge region and one is located in the center region like it was shown in Figure 3a. For the behind configuration, the NPs are only trapped in the center region, and trapping was only observed for high pressures of 183 and 204 Pa. In contrast to that, the middle configuration shows only trapping at the edge regions, and trapping was observed from 141 to 204 Pa. The normal inlet configuration shows a transition from vortex-like trapping at the edge regions (at lower pressures) towards a superposition of both trapping regions (at higher pressures). From 118 to 163 Pa the NPs are only trapped at the edge regions. For 183 and 204 Pa the normal inlet configuration shows trapping at both locations.

For better visualization of the exact positions of the NP trapping regions, the field of view of the camera is divided into 9 quadrants (**Figure 5**a). Then the intensities of the quadrants I and III (representative for edge regions) are summed up and divided by the sum of quadrants V and VIII (representative for center region) for each frame (Figure 5b). This is done because the edge trapping regions are always located in the quadrants I and III. The trapping of NPs in the central region is always located in the quadrants V and VIII. Therefore, for the calculation of the ratio of intensities only the quadrants I, III, V, and VIII are considered. In every time bin, 25 sequential frames are taken to calculate the mean intensity values for regions I, III, V, and VII. One bin contains 1 s of time and the bin 1 s, ranges from 0 to 1 s. For each bin, the ratio of intensities is

 © 2022 The Authors. Particle & Particle Systems Characterization published by Wiley-VCH GmbH

Particle & Particle Systems Characterization
www.particle-journal.com

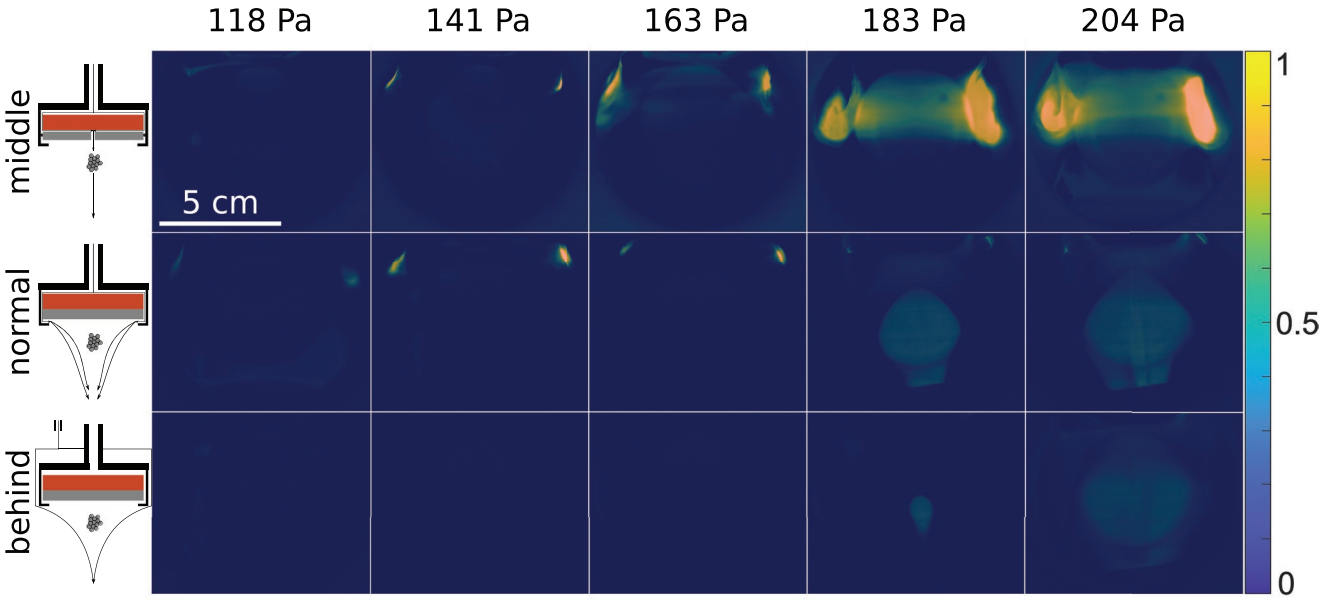

Figure 4. 15 LLS images for different gas inlet configurations and pressures after 30 s of magnetron operation are shown. The pressure is increasing from the left side to the right side. Each row corresponds to one inlet configuration: the first row to the middle inlet, the second to the normal inlet, and the third to the behind inlet. It is visible that for normal configuration NPs are found at the edge regions and also in the center region of the GAS. The middle configuration shows only NP trapping at the edge region. The behind configuration shows NPs only in the center region.

calculated from these mean intensity values. The color scale for the time bins goes from black over red to yellow and represents increasing deposition time. By this method the time dependence of the ratio of intensities becomes visible. If the calculated ratio is clearly smaller than 1, the center regions are dominating. If the ratio is clearly above one, the edge regions are dominating. Assuming that the size distribution of NPs in all quadrants is similar, the ratio gives the information at which position the majority of NPs are located.

Figure 5b shows for the normal configuration, that for a low pressure no clear trend of the location of trapped NPs is present. This is related to the low LLS signal in this experiment. For pressures of 141 and 163 Pa the majority of NPs are clearly located at the edge regions. With increasing time the ratio of intensities increases which shows that more and more NPs are located in the edge regions over time in comparison to the center regions. At higher pressures the trend is different. Here the majority of NPs are trapped at the center region, which is most probably caused by the increasing pressure and flow, which leads to higher drag forces and finally changes the trapping position from the edge regions to the center region.

The behind configuration shows no clear tendency for pressure from 118 to 163 Pa, which is related to the low signal, which can be also seen in Figure 4. For pressures of 183 and 204 Pa the majority of NPs are trapped in the center regions. That no trapping is observed in the behind configuration in the edge regions in contrast to the normal configuration is most probably caused by different gas velocity distribution inside the GAS. CFD simulations have shown, that the velocity is always highest at the inlet and the outlet orifice.[32–36] In regions, which are not in the direct path between inlet and outlet the velocity is small. For the normal configuration, a low velocity at the edge regions can be assumed. In contrast to that, the velocity for the behind configuration will be higher. Therefore, less or no trapping is expected for the behind configuration at the edge regions, which the experiments also proved.

For the middle configuration for pressures higher than 141 Pa, the majority of NPs were always at the edge regions. For the lowest pressure of 118 Pa again no clear trend is visible, which is also related to the low LLS signal. The reason for the trapping at the edge regions for this inlet configuration is also explained by the gas velocity distribution. The highest gas velocity is expected in the center of the gas since the gas inlet and outlet are located in the central axis of the GAS. Therefore, trapping in the center is unexpected, as the LLS results have successfully shown.

3.3. Influence of Gas Inlet and Gas Flow/Pressure on the NP Size Distribution

In this part of the study, the influence of gas flow, pressure, and inlet configuration on the size distribution of the deposited NPs will be discussed. It will be shown that the mean diameter of the deposited NPs does not exhibit the same trend for all inlet configurations in dependence on the gas flow/pressure. **Figure 6** shows six size distributions with corresponding SEM images as insets. The left column corresponds to a pressure of 118 Pa and the right column to 204 Pa. The first row corresponds to the middle inlet configuration, the second row to the normal configuration, and the last row to the behind inlet configuration It is important to note that for the middle inlet row, for the normal inlet for a pressure of 204 Pa and for the behind inlet for a pressure of 204 Pa the largest NPs are not visible in the distribution. Their size is shown directly in the SEM

© 2022 The Authors. Particle & Particle Systems Characterization published by Wiley-VCH GmbH

15214117, 2022, 11, Downloaded from https://onlinelibrary.wiley.com/doi/10.1002/ppsc.202200112 by Universitatsbibliothek Kiel, Wiley Online Library on [19/05/2023]. See the Terms and Conditions (https://onlinelibrary.wiley.com/terms-and-conditions) on Wiley Online Library for rules of use; OA articles are governed by the applicable Creative Commons License

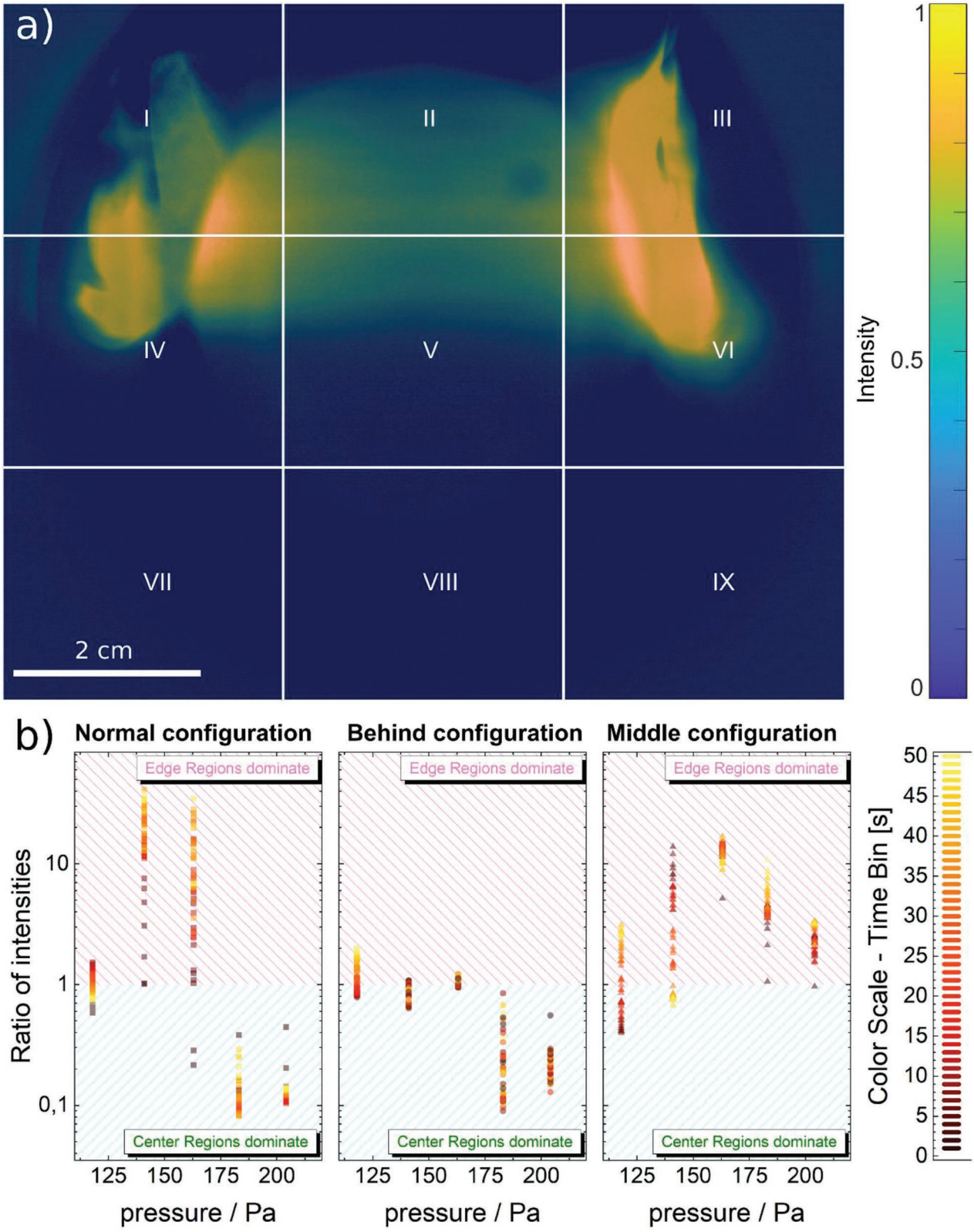

Figure 5. a) Exemplary LLS image for the middle configuration with a pressure of 183 Pa after 30 s of operation. The picture is divided into 9 quadrants. The labeling of the quadrants is important for following calculations. b) The plot shows the ratio of intensities vs. pressure for the three different types of gas inlets. The intensities of the quadrants I and III are summed up and divided by the sum of quadrants V and VIII for each bin. For each bin, the intensities of 25 sequential frames are considered, which corresponds to 1 s. The color scale goes from black (first time bin) over red to yellow and represents an increasing bin number, which is proportional to increasing deposition time (b).

© 2022 The Authors. Particle & Particle Systems Characterization published by Wiley-VCH GmbH

15214117, 2022, 11, Downloaded from https://onlinelibrary.wiley.com/doi/10.1002/ppsc.202200112 by Universitatsbibliothek Kiel, Wiley Online Library on [19/05/2023]. See the Terms and Conditions (https://onlinelibrary.wiley.com/terms-and-conditions) on Wiley Online Library for rules of use; OA articles are governed by the applicable Creative Commons License

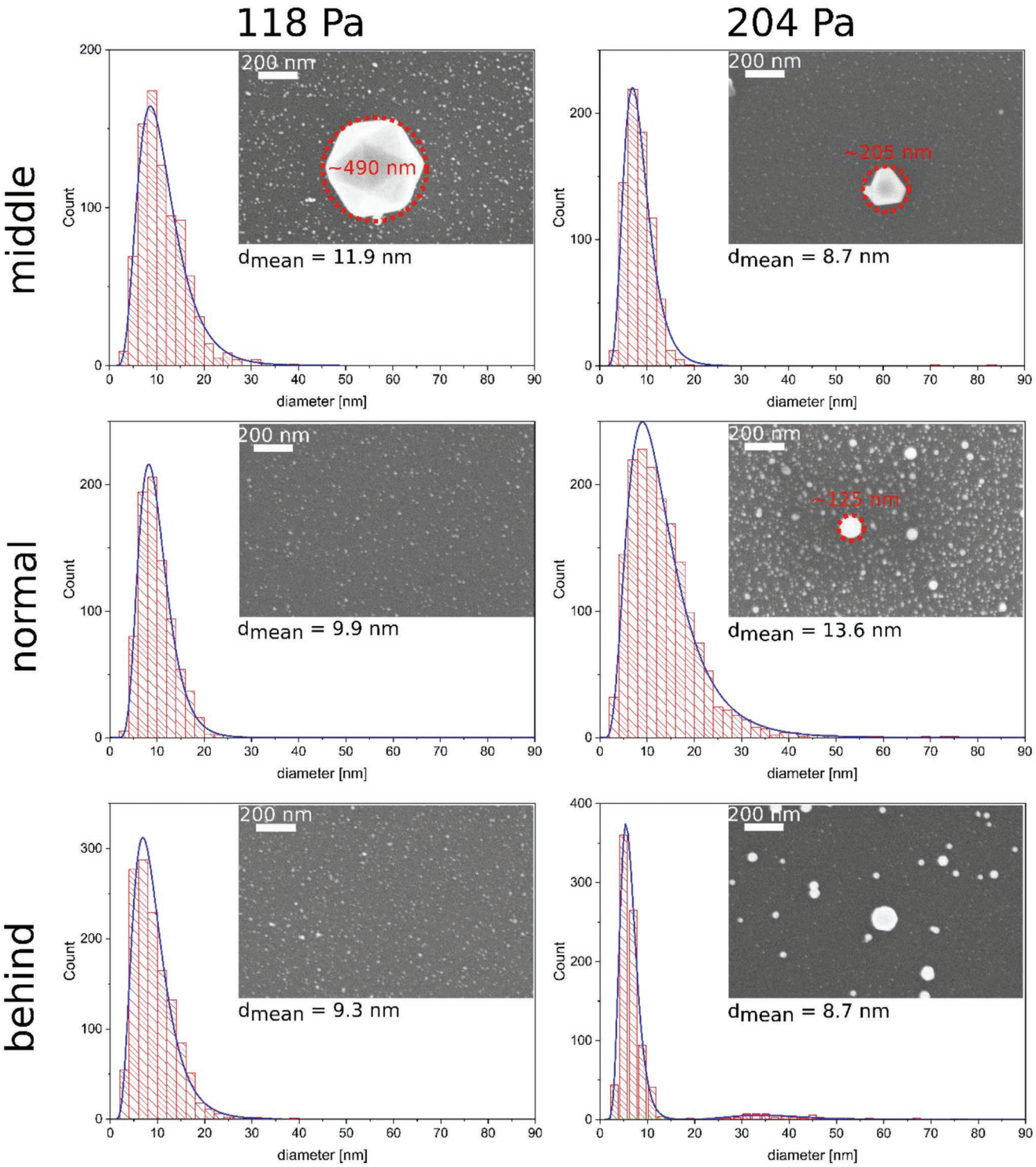

Figure 6. Size distributions and SEM micrographs as insets for two different flows for each type of gas inlet configuration. The left column corresponds to pressure of 118 Pa and the right to 204 Pa. The first row corresponds to the middle gas inlet, the second to the normal gas inlet, and the last one to the behind gas inlet. Additionally, the mean diameter of the size distribution is depicted in the histograms.

pictures because the visibility of the size distributions would be worsened when these particles would be included.

In general, for all gas configurations and pressures log normal distributions are obtained except the behind configuration, which shows a bimodal log normal distribution for a pressure of 204 Pa. All fitting parameters, the mean value, and the fitting function for all size distributions are presented in Table S1 and Equation S1, Supporting Information. When

© 2022 The Authors. Particle & Particle Systems Characterization published by Wiley-VCH GmbH

15214117, 2022, 11, Downloaded from https://onlinelibrary.wiley.com/doi/10.1002/ppsc.202200112 by Universitatsbibliothek Kiel, Wiley Online Library on [19/05/2023]. See the Terms and Conditions (https://onlinelibrary.wiley.com/terms-and-conditions) on Wiley Online Library for rules of use; OA articles are governed by the applicable Creative Commons License

comparing the mean values of the distributions, the normal configuration shows an increase from 9.9 to 13.6 nm. In contrast to that, the mean for the middle configuration and the behind configuration is decreasing from lower to higher pressure. The mean for the middle configuration decreases from 11.9 to 8.7 nm and for the behind configuration from 9.3 to 8.7 nm.

This behavior of the NPs size is counter-intuitive because one would expect the same trend of the size distribution with increasing flow/pressure for all inlet configurations. This shows once more how important the influence of the gas inlet configuration is. The literature explanation for the flow/ pressure dependence on the NPs' size is, that for an increase in Ar flow/pressure the mean NP size and broadness of the distribution is firstly increasing and after a maximum at higher flow decreasing again. This is related to the more effective nucleation with higher pressures in the beginning. At higher flows, the reduced residence time stops the growth of NPs at earlier stages and reduces the probability for coalescence of NPs, which leads to smaller NP sizes.[49–51] From this explanation one would expect the same trend for all gas inlets, but the results indicate different behaviors for different gas inlets.

Although most of the NPs have a size of around 11.9 nm, the middle inlet configuration additionally shows a pressure of 118 Pa, an NP with a diameter of ≈490 nm and for a pressure of 204 Pa, an NP of ≈205 nm in the examined region (20 μm^2). The shape suggests that these NPs are monocrystalline due to crystalline facets. A diameter of ≈490 nm was never produced before in our experiments with normal gas inlets inside a Haberland-type GAS. In the Supporting Information, SEM pictures with lower magnifications are shown (Figure S1, Supporting Information). They show that in the observed region for the middle inlet configuration for a pressure of 118 Pa, indeed, only one NP with a diameter of ≈490 nm was found. On the other hand, for a pressure of 204 Pa more NPs with diameters larger than 100 nm were found in the analyzed area.

The different trends in the flow/pressure dependence on the gas inlet position and also the observation of large NPs (greater than 200 nm) for the middle inlet configuration can be explained perhaps with different gas velocity distributions inside the GAS for different gas inlets. CFD simulations in other publications have shown that a broad velocity distribution is present inside the GAS and that also vortex regions can be present. The simulations have also shown that the highest velocity was always found at the inlet and outlet of the gas.[32–36] Since the gas inlet position was varied, a different gas velocity distribution is expected for all gas inlet configurations. This can cause different release probabilities for the trapped NPs in the GAS.

In the middle configuration, for example, the trapping regions are in the edge regions. Here it is most probably more difficult for NPs to escape and get deposited onto the substrate. It is possible that the larger NPs with diameters above 200 nm are originating from these regions. For the normal and behind configuration one trapping region is in the center. These NPs may escape more often than NPs in the edge regions. Since the residence time of trapped NPs is higher, they have more time to grow. This is perhaps the reason why the size distributions are also showing different trends depending on the gas inlet and pressure. This potentially also explains the bimodal distribution for the behind inlet at a pressure of 204 Pa. This shows once more how important the gas inlet and fluid dynamics are inside a GAS.

3.4. Impact of Gas Inlet and Gas Flow/Pressure on the Deposition Rate

After the effect of different gas inlets and pressures on the location of trapped NP and their size distributions were discussed in the last section, we will show how the deposition rate is influenced by the different gas inlet geometries and gas flows and pressures. To determine the deposition rate, a QCM is used. The change in the resonance frequency of the QCM crystal is directly proportional to the deposited mass and, therefore, to the mass of deposited NPs. **Figure 7** shows the absolute difference in frequency of the QCM for a deposition of 60 s for all inlet configurations in dependence on the pressure. It is obvious that for all inlet configurations the deposited mass for increasing from 118 to 183 Pa. Up to a pressure of 183 Pa, the behind configuration has a higher deposited mass in comparison to the other configurations. The middle inlet configuration shows the lowest deposited mass in this pressure interval. For 204 Pa all configurations are showing a drastic increase in the deposited mass. The configuration with the highest deposited mass is the middle configuration with 521 Hz, followed by the normal inlet with 212 Hz, followed by the behind inlet with 128 Hz. The general increase of deposition rate with increasing flow and pressure for all configurations can be explained by better NP growth conditions and better NP transport.[52] But this does not explain why the behind configuration up to a pressure of 183 Pa always shows higher deposition rates than the other configurations. This must be related to less NP trapping for the behind configuration in comparison to the other

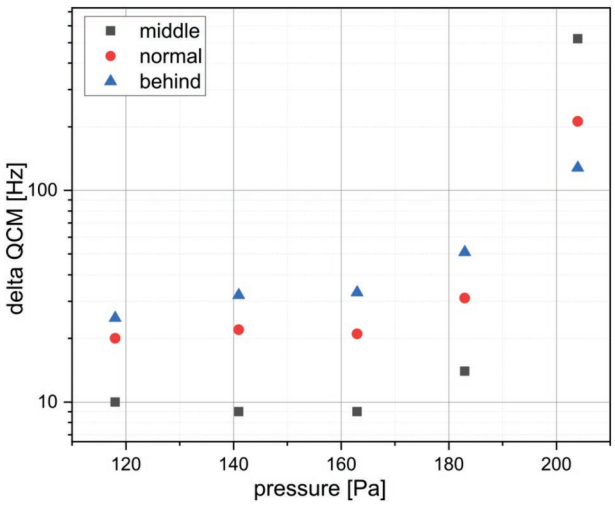

Figure 7. The left plot shows the delta QCM value (absolute difference in frequency after 60 s deposition time) vs. the pressure for all types of inlet configurations. The absolute difference in frequency is directly proportional to the deposited mass. It is obvious that for all inlet configurations the deposited mass is increasing from 118 to 183 Pa. For 204 Pa all configurations are showing a drastic increase in the deposited mass.

© 2022 The Authors. Particle & Particle Systems Characterization published by Wiley-VCH GmbH

15214117, 2022, 11, Downloaded from https://onlinelibrary.wiley.com/doi/10.1002/ppsc.202200112 by Universitatsbibliothek Kiel, Wiley Online Library on [19/05/2023]. See the Terms and Conditions (https://onlinelibrary.wiley.com/terms-and-conditions) on Wiley Online Library for rules of use; OA articles are governed by the applicable Creative Commons License

15214117, 2022, 11, Downloaded from https://onlinelibrary.wiley.com/doi/10.1002/ppsc.202200112 by Universitatsbibliothek Kiel, Wiley Online Library on [19/05/2023]. See the Terms and Conditions (https://onlinelibrary.wiley.com/terms-and-conditions) on Wiley Online Library for rules of use; OA articles are governed by the applicable Creative Commons License

configurations, which is in line with the results from the LLS measurements (Section 3.2).

The reason for this behavior can be explained by the gas flow. In the middle configuration, the highest gas velocity can be assumed to be in the center region of the GAS from the inlet to the orifice. On the other hand, the gas velocity at the sides will be much lower. This means that the drag force which can release the particles from the GAS is in the center much higher in comparison to the edge regions. NPs which are located at the edge regions are not efficiently dragged to the orifice in comparison to the NPs in the center. Figure 4 shows clearly that in the middle configuration particles are only trapped at the edge regions and not in the center region.

Comparing this behavior with the behind configuration, the strongest difference is that no NP trapping at the edge regions of the GAS occurs, because in the edge regions the gas velocity, and so the drag force, is higher in relation to the middle inlet (Figure 4). Also, the deposited mass is higher up to 183 Pa for the behind configuration than for the middle configuration (Figure 7). This indicates that trapping is less pronounced in this configuration in comparison to the middle configuration.

The position of the trapping regions for the normal inlet configuration is of interest, too. Up to a pressure of 163 Pa, the NP are predominantly trapped at the sides. For higher pressures, the signal in this trapping region is reduced and a new trapping zone in the bottom center appears. It is clear that due to different GAS inlet configuration, the gas velocity is low at the edges in comparison to the behind configuration. But in the center, the velocity is most probably still lower in comparison to the middle configuration.

At 204 Pa the order of the gas inlets with the maximum deposition rate is changing. Here, the middle inlet shows the highest deposition rate, followed by the normal inlet and then the behind inlet. The middle inlet shows the highest deposition rate, which may be caused by stronger turbulences inside the GAS. This may affect NPs from the edge regions leaving the trapping by too high centrifugal forces, which push them into the central regions where the gas flow guides them to the orifice. This is perhaps also the explanation for the higher deposition rate of the normal inlet in comparison to the behind inlet configuration for a pressure of 204 Pa. Because also for the normal inlet configuration still NP trapping was observed in the edge regions. Interestingly the finding, that the behind configuration showed up to a pressure of 183 Pa always a higher deposition rate in comparison to the normal inlet, is contrary to the findings by Sanzone et. al.[32] They observed that the deposition rate of Au NPs for a normal configuration was 20 times higher compared to behind inlet even though the sputtering power was roughly 4 times higher for the behind configuration (31 W vs. 8 W). The observed different outcomes can be potentially traced back to differences in the source geometry as well as the applied DC power (300 W in this study compared to 31 or 8 W in the work by Sanzone et. al.). On the one hand, a change in power strongly affects the plasma parameters, which can lead finally to a variation of the trapping forces acting on the NPs. On the other hand, Sanzone et. al. observed a strong increase from 8 to 31 W in the deposition rate for the normal configuration. This indicates that the nucleation process was most probably not extremely efficient at the lower power settings. The reason could be, that for low power fewer sputtered atoms are present in the aggregation volume, which reduces the probability for three-body collisions. These aspects are expected to severely impact the trapping forces and the nucleation process, which may explain the observed different results. Taken all together, the middle inlet seems to produce more efficient trapping in comparison to the behind and normal inlet. This is caused by different gas velocity distributions inside the GAS. To reduce the amount of trapping it would be beneficial to design an inlet configuration where the gas enters the GAS at the middle inlet and also from behind the magnetron. This would reduce the trapping regions and can increase the overall deposited mass and material conversion efficiency. Additionally, the general source dimension and geometry can potentially be improved with the help of CFD simulations, which aid the prediction of low-velocity regions inside the source during the design process. One option for future improvements could be to decrease the diameter of the source to nearly the diameter of the ground cap of the magnetron. In this case, the development of trapping regions, which were observed in the edge regions would be impeded by the constrained GAS dimensions. This may prevent trapping in these regions, but simultaneously may cause more sputtered atoms to be deposited onto the chamber walls, which in turn would reduce the efficiency of the GAS. Here, CFD simulations combined with experimental tests should allow to find the optimum geometry.

4. Conclusion and Outlook

NP formation and transport inside a GAS are highly dynamic processes. A deeper understanding of the gas phase synthesis in a magnetron-based GAS requires elaborate in situ diagnostic methods. This study demonstrates how LLS can be applied to obtain in situ time-resolved information on the location of NP trapping. In the future, the LLS technique could be improved by light sources with different and smaller wavelengths to estimate the sizes of the trapped NPs. Additionally, more powerful light sources and a better camera, with a high frame rate and a low exposure time, could be used to learn more about the forces acting on the NPs, if the release could be monitored when the plasma is switched off.

Nevertheless, the LLS results have shown that NPs are trapped in different regions inside a GAS. The trapping position and LLS intensity of NPs inside the gas depend strongly on the gas flow and pressure. Additionally, three different gas inlet configurations and their impact on the NP trapping were studied. It turned out, that the location of the gas inlet is the most important parameter, which affects the confinement and the size distribution of NPs. The middle inlet showed the strongest trapping of NPs with a vortex-like behavior. However, the position of the trapping was only at the edge regions, which was also expectable because of the high gas velocity in the center of the source. This indicates that this configuration is perhaps not the most efficient gas inlet configuration for a GAS. Nevertheless, it has also shown how efficiently the gas inlet position can change the trapping behavior and the size distribution of the resulting NPs. Even when only three types of gas inlet locations were investigated in this work, many options

 © 2022 The Authors. Particle & Particle Systems Characterization published by Wiley-VCH GmbH

15214117, 2022, 11, Downloaded from https://onlinelibrary.wiley.com/doi/10.1002/ppsc.202200112 by Universitatsbibliothek Kiel, Wiley Online Library on [19/05/2023]. See the Terms and Conditions (https://onlinelibrary.wiley.com/terms-and-conditions) on Wiley Online Library for rules of use; OA articles are governed by the applicable Creative Commons License

are possible to improve the transport of NPs inside the GAS. Different kinds of inlet configurations can be used to prevent NP trapping or even make use of the trapping to tailor the properties of the resulting NPs. A combination of the LLS technique, together with in situ UV–Vis or in situ SAX and CFD simulations may enable the development of a novel and highly efficient GAS.

Supporting Information

Supporting Information is available from the Wiley Online Library or from the author.

Acknowledgements

Funded by the Deutsche Forschungsgemeinschaft (DFG, German Research Foundation) – Project IDs 411452476; 434434223.

Open access funding enabled and organized by Projekt DEAL.

Conflict of Interest

The authors declare no conflict of interest.

Author Contributions

J.D., A.V., S.R., T.S. H.K., and F.F. developed the idea and conceived the initial design of the study. J.D. and S.R. established the experimental setup and constructed the magnetron with different gas inlets. J.D. performed the Ag NP depositions, recorded the LLS videos, and performed the SEM measurements. J.D. developed the Matlab code for the processing of the LLS videos. J.D. and A.V. analyzed the results and prepared the manuscript draft. A.V. and F.F. supervised the work of J.D. All authors discussed the experimental results and their analysis and revised and approved the manuscript.

Data Availability Statement

The data that support the findings of this study are available from the corresponding author upon reasonable request.

Keywords

dusty plasma, gas aggregation source, gas phase synthesis, in situ laser light scattering, nanoparticles, trapping

Received: June 8, 2022
Revised: July 14, 2022
Published online: July 28, 2022

[1] D. Astruc, *Chem. Rev.* **2020**, *120*, 461.
[2] S. Veziroglu, J. Hwang, J. Drewes, I. Barg, J. Shondo, T. Strunskus, O. Polonskyi, F. Faupel, O. C. Aktas, *Mater. Today Chem.* **2020**, *16*, 100251.
[3] A. Vahl, S. Veziroglu, B. Henkel, T. Strunskus, O. Polonskyi, O. C. Aktas, F. Faupel, *Materials* **2019**, *12*, 2840.
[4] H. Li, Z. Li, Y. Yu, Y. Ma, W. Yang, F. Wang, X. Yin, X. Wang, *J. Phys. Chem. C* **2017**, *121*, 12071.
[5] C. Minnai, M. di Vece, P. Milani, *Nanotechnology* **2017**, *28*, 355702.
[6] C. Minnai, A. Bellacicca, S. A. Brown, P. Milani, *Sci. Rep.* **2017**, *7*, 7955.
[7] M. Mirigliano, D. Decastri, A. Pullia, D. Dellasega, A. Casu, A. Falqui, P. Milani, *Nanotechnol.* **2020**, *31*, 234001.
[8] M. Mirigliano, F. Borghi, A. Podestà, A. Antidormi, L. Colombo, P. Milani, *Nanoscale Adv.* **2019**, *1*, 3119.
[9] Z. Wang, S. Joshi, Savel'ev, H. Jiang, R. Midya, P. Lin, M. Hu, N. Ge, J. P. Strachan, Z. Li, Q. Wu, M. Barnell, G. L. Li, H. L. Xin, R. S. Williams, Q. Xia, J. J. Yang, *Nat. Mater.* **2017**, *16*, 101.
[10] H. Jiang, D. Belkin, S. E. Savel'Ev, S. Lin, Z. Wang, Y. Li, S. Joshi, R. Midya, C. Li, M. Rao, M. Barnell, Q. Wu, J. J. Yang, Q. Xia, *Nat. Commun.* **2017**, *8*, 882.
[11] B. J. Choi, A. C. Torrezan, K. J. Norris, F. Miao, J. P. Strachan, M. X. Zhang, D. A. A. Ohlberg, N. P. Kobayashi, J. J. Yang, R. S. Williams, *Nano Lett.* **2013**, *13*, 3213.
[12] V. Postica, A. Vahl, D. Santos-Carballal, T. Dankwort, L. Kienle, M. Hoppe, A. Cadi-Essadek, N. H. de Leeuw, M. I. Terasa, R. Adelung, F. Faupel, O. Lupan, *ACS Appl. Mater. Interfaces* **2019**, *11*, 31452.
[13] Y. Yong, C. Li, X. Li, T. Li, H. Cui, S. Lv, *J. Phys. Chem. C* **2015**, *119*, 7534.
[14] S. W. Choi, A. Katoch, G. J. Sun, S. S. Kim, *Sens. Actuators, B* **2013**, *181*, 446.
[15] F. Fan, J. Zhang, J. Li, N. Zhang, R. R. Hong, X. Deng, P. Tang, D. Li, *Sens. Actuators, B* **2017**, *241*, 895.
[16] K. Hassan, G. S. Chung, *Sens. Actuators, B* **2017**, *239*, 824.
[17] R. Ferrando, J. Jellinek, R. L. Johnston, *Chem. Rev.* **2008**, *108*, 845.
[18] B. Choi, H.-H. Lee, S. Jin, S. Chun, S.-H. Kim, *Nanotechnology* **2007**, *18*, 075706.
[19] X.-F. Zhang, Z.-G. Liu, W. Shen, S. Gurunathan, *Int. J. Mol. Sci.* **2016**, *17*, 1534.
[20] S. Gurunathan, K. Kalishwaralal, R. Vaidyanathan, D. Venkataraman, S. R. K. Pandian, J. Muniyandi, N. Hariharan, S. H. Eom, *Colloids Surf., B* **2009**, *74*, 328.
[21] J. Drewes, A. Vahl, N. Carstens, T. Strunskus, O. Polonskyi, F. Faupel, *Plasma Processes Polym.* **2020**, *8*, 1.
[22] N. Alissawi, V. Zaporojtchenko, T. Strunskus, I. Kocabas, V. S. K. Chakravadhanula, L. Kienle, D. Garbe-Schönberg, F. Faupel, *Gold Bull.* **2013**, *46*, 3.
[23] M. Petr, O. Kylián, A. Kuzminova, J. Kratochvíl, I. Khalakhan, J. Hanuš, H. Biederman, *Opt. Mater.* **2017**, *64*, 276.
[24] H. T. Beyene, V. S. K. Chakravadhanula, C. Hanisch, M. Elbahri, T. Strunskus, V. Zaporojtchenko, L. Kienle, F. Faupel, *J. Mater. Sci.* **2010**, *45*, 5865.
[25] M. Gensch, M. Schwartzkopf, W. Ohm, C. J. Brett, P. Pandit, S. K. Vayalil, L. Bießmann, L. P. Kreuzer, J. Drewes, O. Polonskyi, T. Strunskus, F. Faupel, A. Stierle, P. Müller-Buschbaum, S v. Roth, *ACS Appl. Mater. Interfaces* **2019**, *11*, 29416.
[26] M. T. Nguyen, T. Yonezawa, *Sci. Technol. Adv. Mater.* **2018**, *19*, 883.
[27] M. T. Nguyen, T. Yonezawa, Y. Wang, T. Tokunaga, *Mater. Lett.* **2016**, *171*, 75.
[28] M. Meischein, M. Fork, A. Ludwig, *Nanomaterials* **2020**, *10*, 525.
[29] S. Vučković, M. Svanqvist, V. N. Popok, *Rev. Sci. Instrum.* **2008**, *79*, 073303.
[30] H. Haberland, M. Karrais, M. Mall, Y. Thurner, *JourJ. Vac. Sci. Technol., A* **1992**, *10*, 3266.
[31] P. Grammatikopoulos, *Curr. Opin. Chem. Eng.* **2019**, *23*, 164.
[32] G. Sanzone, J. Yin, K. Cooke, H. Sun, P. Lievens, *Rev. Sci. Instrum.* **2021**, *92*, 033901.
[33] D. Nikitin, J. Hanuš, S. Ali-Ogly, O. Polonskyi, J. Drewes, F. Faupel, H. Biederman, A. Choukourov, *Plasma Processes Polym.* **2019**, *16*, 1900079.

 © 2022 The Authors. Particle & Particle Systems Characterization published by Wiley-VCH GmbH

[34] D. Nikitin, J. Hanuš, P. Pleskunov, Z. Krtouš, S. Ali-Ogly, R. Tafiichuk, K. Biliak, M. Protsak, J. Valter, J. Vyskočil, A. Choukourov, H. Biederman, *Plasma Processes Polym.* **2021**, *16*, 1.
[35] R. Rudd, A. Obrusník, P. Zikán, R. Pratt, C. Hall, P. Murphy, D. Evans, E. Charrault, *Surf. Coat. Technol.* **2016**, *314*, 125.
[36] J. Drewes, S. Ali-Ogly, T. Strunskus, T. Polonskyi, H. Biederman, F. Faupel, A. Vahl, *Plasma Processes Polym.* **2021**, 2100125.
[37] J. Kousal, A. Shelemin, M. Schwartzkopf, O. Polonskyi, J. Hanuš, P. Solař, M. Vaidulych, D. Nikitin, P. Pleskunov, Z. Krtouš, T. Strunskus, F. Faupel, S v. Roth, H. Biederman, A. Choukourov, *Nanoscale.* **2018**, *10*, 18275.
[38] A. Shelemin, P. Pleskunov, J. Kousal, J. Drewes, J. Hanuš, S. Ali-Ogly, D. Nikitin, P. Solař, J. Kratochvíl, M. Vaidulych, M. Schwartzkopf, O. Kylián, O. Polonskyi, T. Strunskus, F. Faupel, S v. Roth, H. Biederman, A. Choukourov, *Part. Part. Syst. Charact.* **2020**, *37*, 1900436.
[39] I. Pilch, F. Greiner, *J. Appl. Phys.* **2017**, *121*, 113302.
[40] F. Greiner, J. Carstensen, N. Köhler, I. Pilch, H. Ketelsen, S. Knist, A. Piel, *Plasma Sources Science, Technology* **2012**, *21*, 065005.
[41] F. Greiner, A. Melzer, B. Tadsen, S. Groth, C. Killer, F. Kirchschlager, F. Wieben, I. Pilch, H. Krüger, D. Block, A. Piel, S. Wolf, *Eur. Phys. J. D* **2018**, *72*, 81.
[42] Y. Qin, U. R. Kortshagen, E. S. Aydil, *J. Phys. D: Appl. Phys.* **2016**, *49*, 085203.
[43] M. Mikikian, M. Cavarroc, L. Couëdel, Y. Tessier, L. Boufendi, *Pure Appl. Chem.* **2010**, *82*, 1273.
[44] Z. Marvi, E. von Wahl, T. Trottenberg, H. Kersten, *J. Appl. Phys.* **2020**, *127*, 173301.
[45] F. M. J. H. van de Wetering, R. J. C. Brooimans, S. Nijdam, J. Beckers, G. M. W. Kroesen, *J. Phys. D: Appl. Phys.* **2015**, *48*, 035204.
[46] J. Drewes, S. Ali-Ogly, T. Strunskus, O. Polonskyi, H. Biederman, F. Faupel, A. Vahl, *Plasma Processes Polym.* **2022**, *19*, 2100125.
[47] C. Z. Huang, J. Ling, J. Wang, in *Elastic Light Scattering Spectrometry*, De Gruyter, Berlin, Boston **2018**, p. 11.
[48] J. Vernieres, S. Steinhauer, J. Zhao, A. Chapelle, P. Menini, N. Dufour, R. E. Diaz, K. Nordlund, F. Djurabekova, P. Grammatikopoulos, M. Sowwan, *Adv. Funct. Mater.* **2017**, *27*, 1605328.
[49] M. Gracia-Pinilla, E. Martínez, G. S. Vidaurri, E. Pérez-Tijerina, *Nanoscale Res. Lett.* **2010**, *5*, 180.
[50] M. Ganeva, T. Peter, S. Bornholdt, H. Kersten, T. Strunskus, V. Zaporojtchenko, F. Faupel, R. Hippler, *Nanoscale Adv.* **2012**, *52*, 881.
[51] D. Nelli, M. Cerbelaud, R. Ferrando, C. Minnai, *Nanoscale Adv.* **2021**, *3*, 836.
[52] K. T. Batková, S. Haviar, P. Mareš, J. Čapek, *Surf. Coat. Technol.* **2021**, *417*, 127196.

© 2022 The Authors. Particle & Particle Systems Characterization published by Wiley-VCH GmbH

15214117, 2022, 11, Downloaded from https://onlinelibrary.wiley.com/doi/10.1002/ppsc.202200112 by Universitatsbibliothek Kiel, Wiley Online Library on [19/05/2023]. See the Terms and Conditions (https://onlinelibrary.wiley.com/terms-and-conditions) on Wiley Online Library for rules of use; OA articles are governed by the applicable Creative Commons License